

## DYNAMICAL BAR-MODE INSTABILITY IN DIFFERENTIALLY ROTATING MAGNETIZED NEUTRON STARS

KAREN D. CAMARDA<sup>1</sup>, PETER ANNINOS<sup>2</sup>, P. CHRIS FRAGILE<sup>3</sup> AND JOSÉ A. FONT<sup>4</sup>

*To appear in ApJ*

### ABSTRACT

This paper presents a numerical study over a wide parameter space of the likelihood of the dynamical bar-mode instability in differentially rotating magnetized neutron stars. The innovative aspect of this study is the incorporation of magnetic fields in such a context, which have thus far been neglected in the purely hydrodynamical simulations available in the literature. The investigation uses the `Cosmos++` code which allows us to perform three-dimensional simulations on a cylindrical grid at high resolution. A sample of Newtonian magneto-hydrodynamical simulations starting from a set of models previously analyzed by other authors without magnetic fields has been performed, providing estimates of the effects of magnetic fields on the dynamical bar-mode deformation of rotating neutron stars. Overall, our results suggest that the effect of magnetic fields is not likely to be very significant in realistic configurations. Only in the most extreme cases are the magnetic fields able to suppress growth of the bar mode.

*Subject headings:* gravitation — hydrodynamics — instabilities — stars: neutron — stars: rotation

### 1. INTRODUCTION

Rotating neutron stars formed following the gravitational collapse of a massive stellar iron core or the accretion-induced collapse of a white dwarf can be subject to various nonaxisymmetric instabilities depending on the amount and degree of differential rotation. The prospects of detection of gravitational radiation from newly born rapidly rotating neutron stars by the current and future generations of kHz-frequency, ground-based gravitational wave interferometers highly motivate the investigation of such instabilities. In particular, if the rotation rate is high enough and shows a high degree of differentiation, the star is subject to the so-called  $m = 2$ , *dynamical* bar-mode instability driven by hydrodynamics and gravity, with  $m$  being the order of the azimuthal nonaxisymmetric fluid mode  $e^{\pm im\varphi}$ . On the other hand, at lower rotation rates gravitational radiation and viscosity can drive a star *secularly* unstable against bar-mode deformation. These two flavors of the bar-mode instability set in when the ratio  $\beta = T/|W|$  of rotational kinetic energy  $T$  to gravitational potential energy  $W$  exceeds a critical value  $\beta_c$ . Early studies with incompressible MacLaurin spheroids in Newtonian gravity showed that the onset of the instability arises when  $\beta_c \sim 0.27$  and  $0.14$  for the dynamical and secular cases, respectively (Chandrasekhar 1969).

Improvements on these simplified analytic models have been achieved through numerical work. Newtonian and general relativistic analyses of the dynamical bar-mode instability are available in the literature, using both simplified models based on equilibrium stellar configurations perturbed with suitable eigenfunctions, and more

involved models for the core collapse scenario. Newtonian hydrodynamical simulations have shown that the value of  $\beta_c$  is quite independent of the stiffness of the equation of state, provided the star is not strongly differentially rotating (see Houser et al. (1994); New et al. (2000); Liu (2002) and references therein). On the other hand, relativistic simulations (Shibata et al. 2000) have yielded a slightly smaller value of the dynamical instability parameter ( $\beta_c \sim 0.24 - 0.25$ ). They have also shown that the dynamics of the process closely resembles that found in Newtonian theory, that is, unstable models with large enough  $\beta$  develop spiral arms following the formation of bars, ejecting mass and redistributing the angular momentum. Further relativistic simulations (Baiotti et al. 2007) have shown the appearance of nonlinear mode-coupling which can limit, and even suppress, the persistence of the bar-mode deformation. It is also worth mentioning that, as the degree of differential rotation becomes higher and more extreme, Newtonian simulations (Shibata et al. 2002, 2003) have also shown that rotating stars are dynamically unstable against bar-mode deformation even for values of  $\beta$  of order 0.01.

Whether the requirements for the development of the instability inferred from numerical simulations are met by the collapse progenitors remains unclear. Observations of surface velocities imply that a large fraction of progenitor cores are rapidly rotating. However, it has been shown that magnetic torques can spin down the core of the progenitor, leading to slowly rotating neutron stars at birth (Spruit & Phinney 1998). The most recent computations of the evolution of massive stars, which include angular momentum redistribution by magnetic torques and spin estimates of neutron stars at birth, lead to core collapse progenitors which do not seem to rotate fast enough to guarantee the unambiguous growth of the canonical bar-mode instability (Heger et al. 2005; Ott et al. 2006). These estimates are in agreement with observed periods of young neutron stars. However, rapidly rotating cores might be produced by an appropriate mixture of high progenitor mass and low metallicity. Recent

<sup>1</sup> Department of Physics and Astronomy, Washburn University, Topeka, KS 66621, USA

<sup>2</sup> Lawrence Livermore National Laboratory, P.O. Box 808, Livermore, CA 94550, USA

<sup>3</sup> Department of Physics and Astronomy, College of Charleston, Charleston, SC 29424, USA

<sup>4</sup> Departamento de Astronomía y Astrofísica, Universidad de Valencia, Dr. Moliner 50, 46100, Burjassot, Valencia, Spain

estimates suggest that about 1% of all stars with masses larger than 10 solar masses will produce rapidly rotating cores (Woosley & Heger 2006). Recent relativistic simulations of a large sample of rotational core collapse models carried out by Dimmelmeier et al. (2008), which include a state-of-the-art treatment of the relevant physics of the collapse phase and realistic precollapse rotational profiles (see also Ott et al. 2007), have shown that the critical threshold of the dynamical bar-mode instability is never surpassed, at least early after core bounce. However, a large set of the models investigated by Ott et al. (2007) and Dimmelmeier et al. (2008) do show that models with sufficiently differential and rapid rotation are subject to the low- $\beta$  instability. In addition it is also worth mentioning the simulations of Baiotti et al. (2008) which show that hypermassive differentially rotating neutron stars form following the merger of low-mass binary neutron stars, when modeled as polytropes. The resulting hypermassive star undergoes a persistent phase of bar-mode oscillations, emitting large amounts of gravitational radiation prior to its delayed collapse to a black hole.

An important piece of physics that the existing numerical work has so far neglected is the presence of magnetic fields. The amplification and emergence of strong magnetic fields in neutron stars from initially weak magnetic field configurations in the pre-collapse stellar cores are currently under investigation (see e.g., Burrows et al. 2007; Cerdá-Durán et al. 2008, and references therein). We note, however, that the weakest point of all existing magneto-rotational core collapse simulations to date is the fact that both the strength and distribution of the initial magnetic field in the core are unknown.

In this paper, we show results from a detailed numerical study of the effects that magnetic fields may have on the dynamical bar-mode instability in differentially rotating magnetized neutron stars. In particular, we investigate how sensitive the onset and development of the instability is to the presence of magnetic fields, as well as the role played by the magnetorotational instability (MRI) and magnetic braking mechanisms to alter the angular momentum distribution in the star and possibly suppress the bar-mode instability. Our study is motivated by the potential astrophysical implications that the presence of strong magnetic fields may have for post-bounce core collapse dynamics and, in turn, for gravitational wave astronomy.

The uncertainty of the strength and distribution of magnetic fields in collapse progenitors is reflected in our somewhat ad hoc parameterization of the field configuration through a large sample of equilibrium models of rapidly and highly differentially rotating neutron stars. Our sample of Newtonian magnetohydrodynamical (MHD) simulations is based upon the set of purely hydrodynamical models previously analyzed by New et al. (2000). The simulations are performed using the covariant (and adaptive mesh refinement) code *Cosmos++* (Anninos & Fragile 2003; Anninos et al. 2003, 2005; Fragile et al. 2005) which allows us to perform three-dimensional simulations on a logarithmically scaled cylindrical grid at high resolution. A number of equilibrium models of rapidly rotating stars with different values of the rotational instability parameter ( $\beta = T/|W|$ ) and magnetic plasma beta ( $\beta_B = P/P_B$ ), and different poly-

tropic equations of state are constructed, introducing also different configurations for the magnetic field distribution (of both poloidal and toroidal varieties) and field strengths. The equilibrium models are perturbed by seeding small random perturbations in order to initiate the onset of the bar-mode deformation.

The organization of the paper is as follows. Section 2 discusses our basic formalism, numerical methods, diagnostics, and the construction of initial data; Section 3 presents our results in two subsections, one for initially toroidal field configurations and one for poloidal. We conclude with a summary and discussion of our results in Section 4.

## 2. FORMALISM, INITIAL DATA, AND DIAGNOSTICS

### 2.1. *Cosmos++* Framework

Although the *Cosmos++* code now includes options to solve the full radiative and conductive MHD equations for Newtonian systems plus multi-species chemical and nuclear reaction networks, we only include here the subset of those equations necessary for the current work. However, see Anninos et al. (2003) for a more complete description of the Newtonian options including radiation, or Anninos et al. (2005) for the general relativistic formulation and a discussion of the various energy formulation options available in the code. In the present study, we use the internal energy (and artificial viscosity,  $A.V.$ ) formulation due to the robustness of the method in tracking adiabats across thin kinematically dominated stellar atmospheres. The relevant equations are sufficiently different than those published in our previous papers (simplified to Newtonian form and generalized to covariant curvilinear grids) that we write them out here for convenience:

$$\frac{\partial(\sqrt{g} \rho)}{\partial t} + \partial_i(\sqrt{g} \rho V^i) = 0, \quad (1)$$

$$\begin{aligned} \frac{\partial(\sqrt{g} S_k)}{\partial t} + \partial_i(\sqrt{g} S_k V^i) &= \left( \frac{S^i S^j}{2\rho} - \frac{B^i B^j}{8\pi} \right) \sqrt{g} \partial_k g_{ij} \\ &+ \frac{1}{4\pi} \partial_i(\sqrt{g} B^i B_k) \\ &- \sqrt{g} \partial_i [(P + P_B) \delta_k^i + Q_k^i] \\ &- \sqrt{g} \rho \partial_k \Phi, \quad (2) \end{aligned}$$

$$\frac{\partial(\sqrt{g} e)}{\partial t} + \partial_i(\sqrt{g} e V^i) = -(P\delta_j^i + Q_j^i) \partial_i(\sqrt{g} V^j), \quad (3)$$

$$\frac{\partial(\sqrt{g} B^k)}{\partial t} + \partial_i(\sqrt{g} B^k V^i) = \sqrt{g} B^i \partial_i V^k - g^{ik} \partial_i \psi, \quad (4)$$

$$\partial_i(\sqrt{g} g^{ij} \partial_j \Phi) = 4\pi G \sqrt{g} \rho, \quad (5)$$

where  $\partial_i \equiv \partial/\partial\xi^i$  represents covariant derivatives in generalized coordinates  $\xi^i$ , and  $\sqrt{g}$  is the determinant of the spatial 3-metric  $g_{ij}$  defining the coordinate system (cylindrical for this work, with a logarithmically scaled radius to achieve greater resolution in the star's interior). Also,  $\rho$  is the fluid density,  $V^k$  is the contravariant fluid velocity,  $S_k = \rho V_k$  is the covariant momentum,  $e$  is the fluid internal energy density,  $Q_j^i$  is the artificial viscosity tensor (here we use the unsplit finite volume version of the scalar viscosity from (Anninos et al. 2005) with  $k_q = 2.0$  and  $k_l = 0.1$ ),  $P$  is the fluid pressure,  $B^k$  is

the contravariant magnetic field vector,  $P_B = B^i B_i / 8\pi$  is the magnetic pressure.  $\Phi$  is the gravitational potential, which is found by solving equation (5) with multipole boundary conditions that include up to 15 spherical harmonics and all corresponding azimuthal moments. In this work, we assume an ideal gas equation of state in the form  $P = (\Gamma - 1)e$ . The MHD equations are derived with the standard assumptions relevant for many astrophysical problems: the system is nonrelativistic and fully ionized, the displacement currents in Maxwell's equations are neglected, the net electric charge is small, and the characteristic length scales are large compared to particle gyroradii scales.

The scalar potential  $\psi$  in the magnetic induction equation (4) is introduced as a divergence cleanser to maintain a divergence-free magnetic field ( $\partial_i(\sqrt{g} B^i) = 0$ ). Options are included in Cosmos to solve any one of the following constraint equations for  $\psi$  (Dedner et al. 2002):

$$\nabla^2 \psi = -\frac{\partial[\partial_i(\sqrt{g} B^i)]}{\partial t} \approx -\frac{\partial_i(\sqrt{g} B^i)}{\Delta t}, \quad (6)$$

$$\psi = -c_p^2 \partial_i(\sqrt{g} B^i), \quad (7)$$

$$\frac{\partial \psi}{\partial t} = -\frac{c_h^2}{c_p^2} \psi - c_h^2 \partial_i(\sqrt{g} B^i), \quad (8)$$

which correspond, respectively, to elliptic, parabolic, and mixed hyperbolic and parabolic constraints. Here  $c_p$  and  $c_h$  are user-specified constants used to regulate the filtering process and weight the relative significance of the hyperbolic and parabolic components. Also the time derivative in equation (6) is approximated as a finite difference with zero divergence at the initial time. For all of the calculations presented in this paper, we use the mixed hyperbolic and parabolic form with parameters  $c_h = 0.2c_{\text{eff}}\Delta x_{\text{min}}/\Delta t$  and  $c_p^2 = 0.3c_h$ , where  $c_{\text{eff}} = 0.4$  is the Courant coefficient,  $\Delta x_{\text{min}}$  is the minimum covariant zone length, and  $\Delta t$  is the evolution time step.

Equations (1) – (5) and (8) are solved in a modified cylindrical coordinate system  $\xi^i = (\eta, z, \phi)$ , where  $\eta = \ln(\varpi + 1)$  is a logarithmic radial coordinate used to concentrate resolution toward the interior of the star, with  $\varpi = r \sin \theta$  being the usual cylindrical radius. With this coordinate choice, the line element for the metric  $g_{ij}$  becomes

$$dl^2 = e^{2\eta} d\eta^2 + dz^2 + (e^\eta - 1)^2 d\phi^2, \quad (9)$$

and  $\sqrt{g} = e^\eta(e^\eta - 1)$ . We consider two different mesh resolutions,  $64^3$  and  $96^3$ , to address the robustness and relative convergence of our results. These are about optimal resolutions for three-dimensional simulations where a large number of parameters are to be explored, particularly with active magnetic fields which increase substantially the computational workload and suffer greater wave speed restrictions on the time step.

## 2.2. Initial Data

### 2.2.1. Rotating Polytropes

We begin by constructing equilibrium models of rapidly rotating polytropic stars using Hachisu's self-consistent field technique (Hachisu 1986). For an initially axisymmetric configuration with angular velocity  $\Omega = \Omega(\varpi)$  that depends only on the distance of the fluid

from the rotation axis ( $\varpi = r \sin \theta$ ), the equilibrium configuration satisfies

$$\Phi + h_0^2 \Psi + H = C_0, \quad (10)$$

where  $h_0$  and  $C_0$  are constants,  $H = \int \rho^{-1} dP$  is the fluid enthalpy,  $\Phi$  is the gravitational potential obtained by solving the Poisson equation (5), and

$$\Psi(\varpi) = -\frac{1}{h_0^2} \int \Omega^2(\varpi) \varpi d\varpi \quad (11)$$

describes the rotational profile of the star. For a polytropic gas with  $P = \kappa \rho^\Gamma = \kappa \rho^{(1+1/N)}$ , we have

$$H = (N + 1)\kappa \rho^{1/N} = \left( \frac{H_{\text{max}}}{\rho_{\text{max},0}^{1/N}} \right) \rho^{1/N}, \quad (12)$$

where  $\rho_{\text{max},0}$  is the initial maximum density.

A variety of rotation profiles can be considered, such as rigid rotation ( $\Omega = \text{const.}$ ), constant linear velocity ( $\Omega = V_0/\varpi$ ), or constant specific angular momentum ( $\Omega = j_0/\varpi^2$ , where  $j$  is the specific angular momentum of the fluid). In our case, we choose a Maclaurin spheroid profile to compare with the earlier work of unmagnetized neutron stars (New et al. 2000)

$$\Omega(\varpi) = h_0 \left[ 1 - \left( 1 - \frac{m(\varpi)}{M} \right)^{2/3} \right] \varpi^{-2}, \quad (13)$$

where  $M$  equals the total mass of the star (spheroid),  $m(\varpi)$  is the mass interior to  $\varpi$ , and

$$h_0 = \frac{5J}{2M} \quad (14)$$

can now be specified in terms of the total angular momentum  $J$  of the star.

The constants  $h_0$  and  $C_0$  in equation (10) are set by an appropriate choice of boundary conditions. Specifically, we require that  $\rho$ ,  $P$ , and  $H$  vanish at the surface of the star. Any two points on the surface of the star can then be used to specify a solution; we choose a point on the equator (point  $A$ ) and one of the poles (point  $B$ ) by specifying the equatorial surface radius  $\varpi_E$  and axis ratio  $z_P/\varpi_E$ , where  $z_P$  is the polar radius. The constants are then given as

$$h_0^2 = -\frac{\Phi(A) - \Phi(B)}{\Psi(A) - \Psi(B)} \quad (15)$$

and

$$C_0 = \Phi(A) + h_0^2 \Psi(A). \quad (16)$$

Finally we must specify  $\Gamma$  (or  $N$ ) and  $\kappa$  (or  $\rho_{\text{max},0}$ ) to close the system of equations. The solution proceeds by guessing an initial distribution for  $\rho$ ; solving equations (5) and (11) for  $\Phi$  and  $\Psi$ , respectively; using equation (10) to set  $H$  and  $H_{\text{max}}$ ; and then using equation (12) to determine a new density distribution. This procedure is repeated iteratively until the solution converges sufficiently (for us, once  $\Delta h_0/h_0$ ,  $\Delta C_0/C_0$ , and  $\Delta H/H$  are all  $\leq 10^{-4}$ ).

The initial data are solved in two-dimensional logarithmic cylindrical coordinates using the same polar and radial resolutions as the full three-dimensional grid that

we use for the production simulations, which we then map (i.e., rotate) azimuthally onto the three-dimensional grid. The quality of solutions is verified by computing the virial error (V.E.) as

$$\text{V.E.} = 2T + W + 3 \int P dV, \quad (17)$$

where  $T$  is the total kinetic energy,  $W$  is the total gravitational potential energy,  $P$  is the thermal pressure and  $dV$  is the volume element. Virial errors in our calculations are small:  $4 \times 10^{-4}$  for the  $\Gamma = 5/3$  cases,  $8 \times 10^{-4}$  for  $\Gamma = 2$ , and  $1.6 \times 10^{-3}$  for  $\Gamma = 3$ . Normalized to the absolute value of the potential energy, we find  $|\text{V.E.}/W| \lesssim 3 \times 10^{-3}$  for all cases.

Once the equilibrium density distribution  $\rho_{\text{EQ}}$  is determined, we apply a small random perturbation of the form  $\rho(R, z, \phi) = \rho_{\text{EQ}}[1 + a_0 f(R, z, \phi)]$ , where  $a_0 = 10^{-2}$  is the perturbation amplitude and  $f$  is a random number between -1 and 1. This perturbation serves as a seed for the bar-mode and magneto-rotational instabilities to grow.

Because MHD codes have difficulty treating pure vacuums, it is necessary to initially fill the regions of the grid outside the star with a low density ( $\rho_{\text{floor}} = 10^{-6} \rho_{\text{max},0}$ ), low energy ( $e_{\text{floor}} = \kappa \rho_{\text{floor}}^{\Gamma} / (\Gamma - 1)$ ), static ( $V^i = 0$ ) background. During the evolution, any time the fluid density or energy attempt to drop below their respective floor values they are reset.

### 2.2.2. Magnetic Fields

In this work, we choose two idealized initial configurations for the magnetic fields, one purely toroidal and one purely poloidal. In all cases the fields are chosen to be initially weak, so that in some sense they simply represent additional perturbations away from the initial equilibrium state. However, it is now well understood that differentially rotating fluids with weak magnetic fields are susceptible to the MRI (Balbus & Hawley 1991). The only criterion required to trigger the MRI is

$$\frac{d\Omega^2}{d \ln \varpi} < 0, \quad (18)$$

a condition which is clearly met inside our model star. Thus, our initially weak magnetic fields can potentially become dynamically important during the evolution (provided we have sufficient resolution to capture the MRI).

The toroidal field case begins with  $B^\eta = B^z = 0$  and

$$B^\phi = \max \left[ 0, C_T \frac{e^{-\Delta\xi^2/(2\sigma^2)} - e^{-0.5}}{\sqrt{2\pi}\sigma} \right], \quad (19)$$

where  $\Delta\xi = |\xi^i - \xi_{\text{loop}}^i|$  is the position offset relative to the location of the central strongest field loop  $\xi_{\text{loop}}^i = (\eta_{\text{loop}}, 0, \phi)$ . The characteristic half-width of the loop is defined as  $\sigma = \varpi_E/8$ , and  $\eta_{\text{loop}}$  is set to either  $\varpi_E/2$  or  $\varpi_E/4$  so that the center of the toroidal loop is initially located at radius  $r_{\text{loop}} \approx 0.65\varpi_E$  or  $r_{\text{loop}} \approx 0.28\varpi_E$ . The normalization constant  $C_T$  is chosen to satisfy our particular choice for  $\beta_{\text{B,min}}$ , the initially lowest value for  $P/P_B$  inside the star. The extra factor of  $e^{-0.5}$  is included to

ensure that the magnetic field is initially confined to the interior of the star.

The poloidal field case begins with  $B^\phi = 0$ . The other two magnetic field components are specified from a magnetic vector potential using the following divergence-free construction:

$$\sqrt{g}B^i = \left[ -\frac{\partial}{\partial z} (\sqrt{g_{\phi\phi}}A_\phi), \quad \frac{\partial}{\partial \eta} (\sqrt{g_{\phi\phi}}A_\phi), \quad 0 \right]. \quad (20)$$

For the vector potential we use the solution corresponding to a current loop in the equatorial plane of radius  $r_{\text{loop}}$  (which we typically set to  $\varpi_E/2$ ) centered on the origin (Jackson 1975)

$$A_\phi = C_P \sum_{n=0}^{\infty} \frac{(-1)^n (2n-1)!!}{2^n (n+1)!} \frac{r_{<}^{2n+1}}{r_{>}^{2n+2}} P_{2n+1}^1(\cos\theta), \quad (21)$$

where  $(2n-1)!! = (2n-1)(2n-3)\dots(5)(3)(1)$ ,  $r_{<} = \min(r, r_{\text{loop}})$ ,  $r_{>} = \max(r, r_{\text{loop}})$ , and  $P_l^m$  are the Legendre polynomials. In practice, we calculate the first 20 terms of the sum. To prevent the magnetic field from extending beyond the surface of the star,  $A_\phi$  is truncated at values smaller than  $0.5A_{\phi,\text{max}}$ , where  $A_{\phi,\text{max}}$  is the maximum value of  $A_\phi$ . Again, the normalization constant  $C_P$  is chosen to satisfy our choice of  $\beta_{\text{B,min}}$ .

As a rough guideline to determine whether there is sufficient numerical resolution to capture the MRI, we compare the grid cell spacing at the position where  $\beta_B = \beta_{\text{B,min}}$  against the characteristic (minimum unstable) MRI wavelength

$$\lambda_{\text{MRI}} = \frac{2\pi v_A}{\Omega}, \quad (22)$$

where  $v_A^2 = 2P_B/\rho$  is the Alfvén velocity of the plasma. The ratio of  $\lambda_{\text{MRI}}$  over the grid spacing  $\Delta\varpi$  at  $\xi^i (\beta_B = \beta_{\text{B,min}})$  is given in Table 1, along with the maximum field amplitude inside the star at the initial time.

### 2.2.3. Grid, Units, and Parameters

In all calculations the radial box size is set to three times the equatorial radius of the star  $L_\varpi = 3\varpi_E$ . The box size along the  $z$ -axis is set smaller than the radial dimension  $L_z = 1.2\varpi_E$ , compensating for the high aspect ratio of the stellar profile while also maintaining reasonable resolution along the  $z$ -axis and accurate multipole boundary conditions for the gravity solver. The logarithmic nature of the coordinate system results in a spatial resolution of  $\Delta\varpi \approx 0.022\varpi_E$  and  $0.014\varpi_E$  near the origin along the radial axis for the  $64^3$  and  $96^3$  grids respectively. This is more than a factor of two improvement in resolution over a uniform grid, and increases the radial resolution to nearly match the polar ( $\Delta z \approx 0.01875\varpi_E$  and  $0.0125\varpi_E$  for the  $64^3$  and  $96^3$  grids). For reference, the azimuthal resolution in the equatorial plane of the  $64^3$  grid varies from  $\varpi\Delta\phi \approx 0.05\varpi_E$  at  $\varpi \sim \varpi_E/2$  to about  $10^{-3}\varpi_E$  near the origin.

Displayed results in all subsequent figures are presented in dimensionless code units. We define the equatorial equilibrium surface radius to be the unit coordinate dimension ( $\tilde{\ell} = \varpi_E = 1.7 \times 10^8$  cm), the dynamical time of a spheroid with equatorial surface radius  $\varpi_E$  to be the unit interval of time ( $\tilde{t} = \sqrt{\varpi_E^3/GM} \approx 0.1$  s for the

$\Gamma = 5/3$  runs), and the maximum central density of the star to be the unit density ( $\bar{\rho} = \rho_{\max,0} = 10^{10}$  g/cm<sup>3</sup>). This in turn implies a scaled magnetic field unit of  $\sqrt{GM\rho_{\max,0}/\varpi_E}$  ( $\approx 1.7 \times 10^{14}$  Gauss for  $\Gamma = 5/3$ ).

Table 1 lists all of the numerical simulations we have performed in this study, together with their corresponding parameter sets. The calculations represent a large parameter space including the field strength characterized by the minimum plasma beta  $\beta_{B,\min}$ , the field orientation (toroidal or poloidal), the equatorial field or current loop radius  $r_{\text{loop}}$ , the equation of state polytropic index  $\Gamma$ , the rotational instability parameter  $\beta$ , the polar to equatorial axis ratio  $A_r$ , and the grid resolution. Also shown in Table 1 is the maximum magnetic field amplitude inside the star, and the ratio of the MRI wavelength over the local radial cell resolution. The prefixes ‘‘T’’ and ‘‘P’’ in our naming convention refer to initial toroidal and poloidal field orientations, respectively. Runs labeled without either of these prefixes are the baseline unmagnetized calculations.

### 2.3. Gravitational Radiation Diagnostic

Because the spacetime metric is held fixed in our simulations, we compute the gravitational radiation produced by these systems in the (traceless) quadrupole approximation. For an observer located on the symmetry axis, the two polarizations of the gravitational wave amplitude are written as

$$h_+ = \frac{G}{c^4} \frac{1}{r} \left( \ddot{I}_{xx} - \ddot{I}_{yy} \right), \quad (23)$$

$$h_\times = \frac{G}{c^4} \frac{2}{r} \ddot{I}_{xy}, \quad (24)$$

where  $\ddot{I}_{ij}$  is second time derivative of the reduced quadrupole moment of the mass distribution, given in flat space Cartesian coordinates  $x^k$  by

$$I_{ij} = \int \rho (x_i x_j - \frac{1}{3} \delta_{ij} r^2) d^3x, \quad (25)$$

and  $r = \sqrt{x^2 + y^2 + z^2}$  is the spherical distance to the source center of mass. The integral is evaluated over the entire mass distribution.

It is well known that the straight-forward procedure of computing the components of  $I_{ij}$  at each time step, and then taking the needed time derivatives of the result numerically, produces an unacceptable level of numerical noise in the resulting waveforms (Finn & Evans 1990). Instead we differentiate equation (25) with respect to time twice, each time using the evolution equations (1) – (4) to replace the time derivatives that appear in the resulting integrand. Many of the spatial derivatives which are introduced by this procedure can then be eliminated using integration by parts. The resulting expression for  $\ddot{I}_{ij}$  is similar to that given in New et al. (2000), except here we include a potential term missing from that expression, and add artificial viscosity and magnetic field

contributions:

$$\begin{aligned} \ddot{I}_{ij} = \int & \left[ 2\rho V_i V_j - \frac{2}{3} \delta_{ij} \rho V^k V_k \right. \\ & - \rho x_j \partial_i \Phi - \rho x_i \partial_j \Phi + \frac{2}{3} \delta_{ij} \rho x^k \partial_k \Phi \\ & - \frac{1}{4\pi} (2B_i B_j - \delta_{ij} B^k B_k) - \frac{2}{3} \delta_{ij} \left( \frac{B^k B_k}{8\pi} \right) \\ & \left. + Q_{ij} + Q_{ji} - \frac{2}{3} \delta_{ij} Q_k^k \right] d^3x. \end{aligned} \quad (26)$$

In the following sections, we present the quantity  $rh_+$ , to scale out the radial dependence, and normalize the wave amplitudes by  $(GM/\varpi_E c^2)^2$  so that a direct comparison can be made to previous unmagnetized calculations.

## 3. RESULTS

### 3.1. Toroidal Magnetic Field Configurations

All calculations with toroidal configurations begin with an initial axisymmetric solution in near equilibrium, and subsequently evolve in a similar fashion. They display the characteristic exponential growth of the even (primarily  $m = 2$  and 4) non-axisymmetric modes at early times, followed by a mode saturation phase during which the star develops an elongated bar structure with spiral arms, then a final bar attenuation phase that redistributes angular momentum as the star evolves into a more axisymmetric configuration again. The early and intermediate phases of the bar-mode growth are illustrated in Figure 1 where we show images of the mass density (for the G53Binf case) and magnetic pressure (for the TG53B100 case) in the equatorial plane. Both sets of images display the same contour levels of the mass density (0.5, 0.05, 0.005, 0.0009) normalized to the initial maximum mass density  $\rho_{\max,0}$ . The mass densities are virtually identical in both magnetized and unmagnetized runs. The magnetic pressure is initially confined within density contour levels 0.05 and 0.5, a region about  $2\sigma = 0.25\varpi_E$  thick in radius. The magnetic field for this configuration is not buoyant but remains mostly confined to those level boundaries as the bar mode takes shape.

Comparing mass density contours from the two simulations in Figure 1, it is apparent that the introduction of magnetic fields (at least for this particular field configuration) does not affect appreciably the growth of the bar mode. This is confirmed in Figure 2 where we compare the growth of the amplitude  $|A_m|$  for the first few non-axisymmetric modes ( $m = 1, 2,$  and 4) in the same two runs as Figure 1 (G53Binf and TG53B100). For reasons of clarity, we do not show the  $m = 3$  curve, but note instead that the overall shape and amplitude are very similar to the  $m = 1$  mode. The quantity  $|A_m|$  plotted in Figure 2 is the same as that introduced in New et al. (2000). It represents the mode amplitude inside a ring centered at a fixed cylindrical radius ( $\varpi = 0.45\varpi_E$ ) in the equatorial plane ( $z = 0$ )

$$|A_m| = \frac{|C_m|}{|C_0|} = \frac{\int_0^{2\pi} \bar{\rho} e^{-im\phi} d\phi}{\int_0^{2\pi} \bar{\rho} d\phi}, \quad (27)$$

where  $\bar{\rho}$  is the density in the ring, averaged over cells along the radial and polar axes as specified by the thickness of the ring in those directions.

TABLE 1  
SIMULATION PARAMETERS

Simulation	Resolution	$\beta_{B,\min}^a$	$\beta^b$	$\Gamma (N)^c$	$A_r^d$	$r_{\text{loop}}^e$	$\lambda_{\text{MRI}}/\Delta\varpi^f$	$ B _{\text{max}}^g$
G53Binf	64 <sup>3</sup>	$\infty$	0.295	5/3 (1.5)	0.208	—	—	—
G53BinfHR	96 <sup>3</sup>	$\infty$	0.295	5/3 (1.5)	0.208	—	—	—
G20Binf	64 <sup>3</sup>	$\infty$	0.286	2 (1.0)	0.250	—	—	—
G30Binf	64 <sup>3</sup>	$\infty$	0.298	3 (0.5)	0.250	—	—	—
TG53B1	64 <sup>3</sup>	1	0.295	5/3 (1.5)	0.208	0.65	35.0	$5.4 \times 10^{13}$
TG53B10	64 <sup>3</sup>	10	0.295	5/3 (1.5)	0.208	0.65	11.0	$1.7 \times 10^{13}$
TG53B100	64 <sup>3</sup>	100	0.295	5/3 (1.5)	0.208	0.65	3.5	$5.4 \times 10^{12}$
TG53B100R3	64 <sup>3</sup>	100	0.295	5/3 (1.5)	0.208	0.28	5.6	$2.9 \times 10^{13}$
TG53B100HR	96 <sup>3</sup>	100	0.292	5/3 (1.5)	0.208	0.65	5.6	$5.5 \times 10^{12}$
TG53B500	64 <sup>3</sup>	500	0.295	5/3 (1.5)	0.208	0.65	1.6	$2.4 \times 10^{12}$
TG53B500R3	64 <sup>3</sup>	500	0.295	5/3 (1.5)	0.208	0.28	2.7	$1.4 \times 10^{13}$
TG53B1e8	64 <sup>3</sup>	1e8	0.295	5/3 (1.5)	0.208	0.65	0.003	$5.4 \times 10^9$
TG20B100	64 <sup>3</sup>	100	0.286	2 (1.0)	0.250	0.65	4.4	$1.8 \times 10^{13}$
TG30B100	64 <sup>3</sup>	100	0.298	3 (0.5)	0.250	0.65	5.2	$4.1 \times 10^{13}$
PG53B10	64 <sup>3</sup>	10	0.295	5/3 (1.5)	0.208	0.5	12.8	$2.3 \times 10^{13}$
PG53B10HR	96 <sup>3</sup>	10	0.292	5/3 (1.5)	0.208	0.5	20.5	$2.7 \times 10^{13}$
PG53B100	64 <sup>3</sup>	100	0.295	5/3 (1.5)	0.208	0.5	4.1	$7.2 \times 10^{12}$
PG53B100HR	96 <sup>3</sup>	100	0.292	5/3 (1.5)	0.208	0.5	6.5	$8.5 \times 10^{12}$
PG53B500	64 <sup>3</sup>	500	0.295	5/3 (1.5)	0.208	0.5	1.8	$3.2 \times 10^{12}$
PG53B500HR	96 <sup>3</sup>	500	0.292	5/3 (1.5)	0.208	0.5	2.9	$3.8 \times 10^{12}$
PG30B100	64 <sup>3</sup>	100	0.298	3 (0.5)	0.250	0.65	6.0	$4.2 \times 10^{13}$

<sup>a</sup>  $\beta_{B,\min} = (P/P_B)_{\min}$  is the plasma parameter defining the minimum hydrodynamic to magnetic pressure ratio (or maximum magnetic field amplitude).

<sup>b</sup>  $\beta = T/|W|$  is the rotational instability parameter.

<sup>c</sup>  $\Gamma = 1 + 1/N$  is the adiabatic index for the ideal gas equation of state.

<sup>d</sup>  $A_r$  is the polar to equatorial axis ratio of the initial star configuration.

<sup>e</sup>  $r_{\text{loop}}$  is the radius of the field or current loop in the equatorial plane.

<sup>f</sup>  $\lambda_{\text{MRI}}/\Delta\varpi$  is the ratio of the MRI wavelength to the (cylindrical) radial cell width ( $\Delta\varpi$ ) at a position corresponding to the minimum initial plasma beta ( $\beta_{B,\min}$ ) inside the star.

<sup>g</sup>  $|B|_{\text{max}}$  is the maximum magnetic field amplitude inside the star in units of Gauss.

An obvious result taken from Figure 2 is the strong similarity in the early exponential growth and late time saturation profiles of both magnetized and unmagnetized runs. But there are also several other points of interest in Figure 2. For example, the  $m = 1$  mode saturates after about five dynamical times to a level that is well below those of the  $m = 2$  and 4 modes (about three orders of magnitude below  $m = 2$ , and two orders below  $m = 4$  at their peaks), as is characteristic of the bar mode. Since the odd modes tend to encapsulate numerical errors such as the center of mass drift and loss of angular momentum, it is encouraging to see the odd modes saturate in time and the characteristic even modes to dominate the Fourier spectrum in convincing fashion. We have tracked the mass center in our calculations and plot the result for a few typical cases in Figure 3. The early drift in the center of mass quickly saturates within a few dynamical times, and the center of mass thereafter remains mostly stationary. The total late-time drift in the position of the star mass center is very small,  $\sim 0.01\varpi_E$  for the 64<sup>3</sup> grids, effectively confined to less than half a cell width in the central most highly resolved (smallest zoning) portion of the grid. The center of mass position is preserved even better in the high-resolution 96<sup>3</sup> runs, being confined to within one quarter of a cell width,  $\sim 0.0025\varpi_E$ .

Although we do not show the results here, we have verified that the modal histories in the magnetized runs are very similar to the unmagnetized results also for the  $\Gamma = 2$  and 3 cases, and both sets look like the  $\Gamma = 5/3$

results in Figure 2. The only major difference that we have observed and attributed to the equation of state is a systematic shift (or delay) in time required for the even bar modes to enter the exponential growth phase. This is discussed further in the paragraphs below in the context of gravitational wave emissions.

The ineffectiveness of toroidal magnetic fields is demonstrated again by two additional calculations in which we varied  $\beta_{B,\min}$  to generate different initial field amplitudes: a factor of five reduction in run TG53B500, and a ten-fold increase in run TG53B10. In both cases, toroidal fields do not affect significantly the growth or development of the bar mode, in spite of the field amplification observed in Figures 4 and 5 which plot the total integrated magnetic energy and the local field amplitude, respectively, as a function of time. The field amplitude in Figure 5 is calculated as an azimuthal average inside a circular annulus in the equatorial plane at radii  $0.65\varpi_E$  (the initial center of the toroidal field loop) and  $0.2\varpi_E$ . Note the field amplitude is already saturated and does not evolve much at the initial configuration radius ( $r_{\text{loop}} = 0.65\varpi_E$ ), but grows substantially at smaller radii. Eventually, the field amplitude and energy saturate in time at all radii to roughly the same value. This behavior is seen in all of the cases we have tried, including the smallest field amplitude case (TG53B1e8) in which the field grows from  $|B| \sim 3 \times 10^{-5}$  to  $\sim 0.02$  at radius  $0.65\varpi_E$  by runs end. A confirmation of the convergence of these results is provided by the

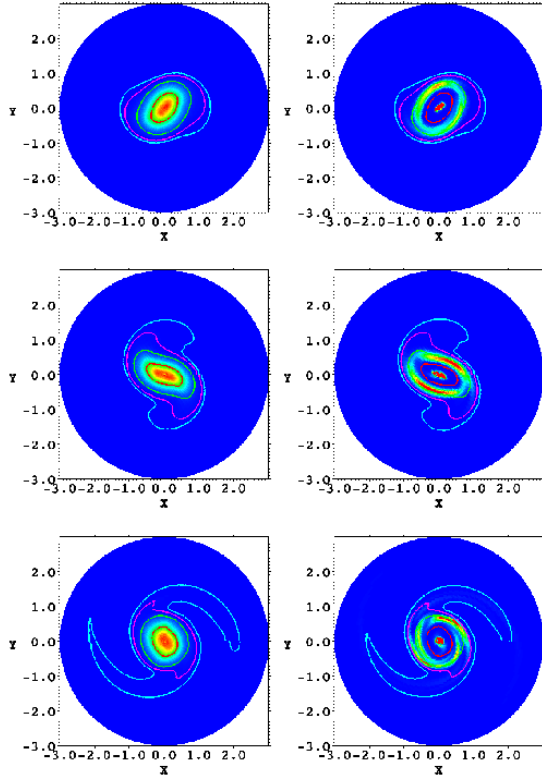


FIG. 1.— Development of the bar mode in the  $\Gamma = 5/3$  simulations with a magnetic field (TG53B100, right column) and without (G53Binf, left column). Rows represent snapshot solutions at times:  $t = 12, 14,$  and  $20$  in dynamical (code) units ( $\tilde{t} = \sqrt{\varpi_E^3/GM}$ ). Contour levels represent mass density in the equatorial plane at four values normalized to the initial maximum density  $\rho_{\max,0}$ : (0.5, 0.05, 0.005, and 0.0009). Linear color maps represent mass density in the case without magnetic fields (left column), and magnetic pressure in the case with fields (right). The magnetic pressure color scale is fixed for all the images to cover the range  $0 \rightarrow 10^{-4}$ . The mass density color scale is adjusted to the maximum density at each time, but does not deviate much from  $0 \rightarrow 1.07$  over all displayed sequences.

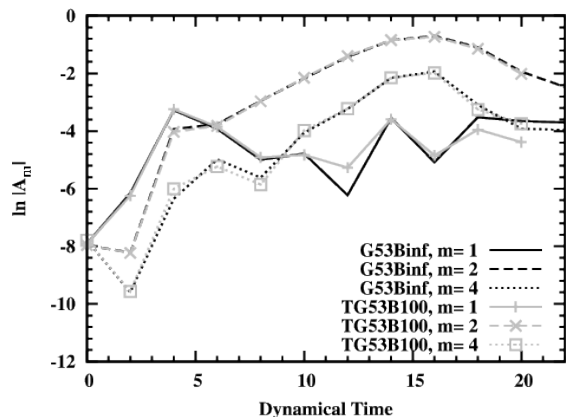


FIG. 2.— Growth of the first few azimuthal Fourier mode amplitudes  $|A_m|$  in the mass density, comparing two  $\Gamma = 5/3$  cases: unmagnetized (G53Binf, dark line types) and magnetized (TG53B100, gray lines and symbols). Results are derived by averaging the density inside a ring centered at  $\varpi = 0.45\varpi_E$  in the equatorial plane, extending one zone deep in both radial and polar directions. We do not plot the  $m = 3$  curve here for reasons of clarity, but note that it roughly tracks the  $m = 1$  curve in shape and amplitude.

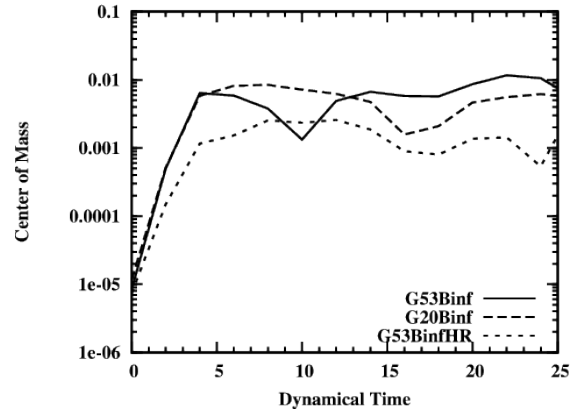


FIG. 3.— Spherical radial position of the center of mass in a few typical unmagnetized runs. The vertical axis is dimensionally normalized by the initial equatorial surface radius  $\varpi_E$ . Apart from a brief drift at early times, the center of mass movement quickly saturates and remains confined to a region that is within a half/quarter cell width radius for the  $64^3/96^3$  grids.

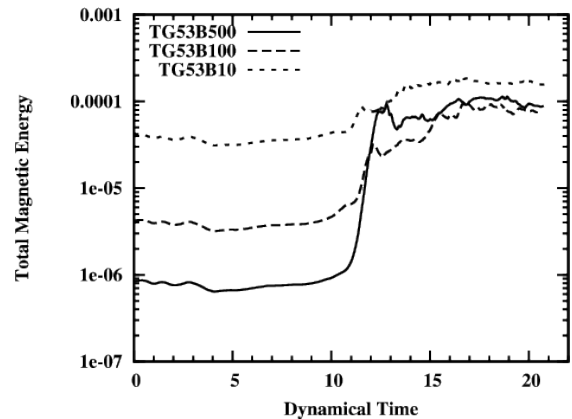


FIG. 4.— Total magnetic energy integrated over the entire grid for a few of the  $\Gamma = 5/3$  cases. The horizontal axis is plotted in dynamical time units  $\sqrt{\varpi_E^3/GM}$ , and the field energy in dimensionless code units.

high-resolution run TG53B100HR which falls between the B10 and B500 results, and tracks closely the corresponding energy and field amplitudes at lower resolution. The only difference between the high and lower resolution curves is the growth phase in the high resolution case is triggered about one dynamical time earlier (approximately a 10% shift in time), but saturates at the same mean field amplitude.

The exponential growth of the magnetic energy around a time  $t \sim 11$  suggests the onset of a powerful magnetic field amplification mechanism. The delayed onset and steep exponential growth particularly favor axisymmetric modes of the MRI. These modes have the shortest growth times, but require a poloidal field component to act upon. For the initially toroidal configurations, significant poloidal fields are not present until the bar mode begins redistributing material within the star, explaining the delayed onset. Furthermore, it is clear from Figures 4 and 5 that the magnetic field saturates to roughly the same level at all radii and for all cases, regardless of initial amplitudes. The saturation level appears comparable to the initial field amplitudes in the B500 case: field amplitudes in cases initially greater than B500 are dissi-

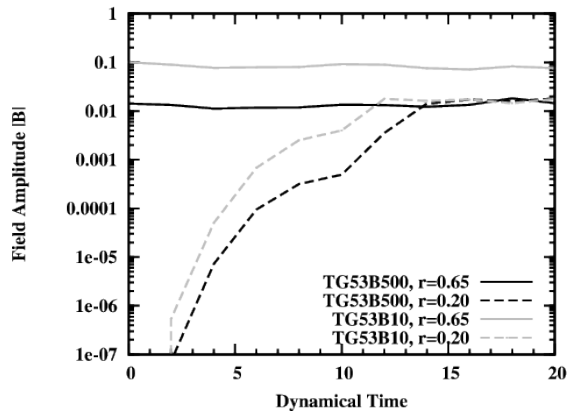


FIG. 5.— Magnetic field amplitude averaged azimuthally inside a circular annulus in the equatorial plane between radii  $0.65\varpi_E$  and  $0.2\varpi_E$ . The horizontal axis is plotted in dynamical time units  $\sqrt{\varpi_E^3/GM}$ , and the field amplitude in dimensionless code units of  $\sqrt{GM\rho_{\max,0}/\varpi_E} \approx 1.7 \times 10^{14}$  Gauss.

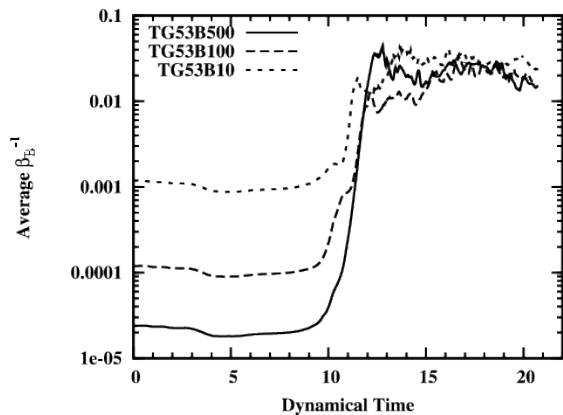


FIG. 6.— Evolution of the mass density weighted average of the inverse of the magnetic plasma beta ( $\beta_B^{-1}$ ) inside the star (satisfied by  $\rho/\rho_{\max} > 10^{-4}$ , where  $\rho_{\max}$  is the maximum density in the star at any given time). The high-resolution run TG53B100HR (not shown here for reasons of clarity) closely resembles the growth curve from the corresponding lower resolution case TG53B100.

pated through hydrodynamic processes; field amplitudes in cases initially less than B500 are amplified until they reach B500 levels before leveling off. Our calculations suggest no mechanism exists which can drive field amplitudes above B500 levels, implying that we are safely modeling the upper limit of self-generated field strengths.

Although field amplification does indeed take place in all magnetized runs we have performed (medium and high resolution), it falls well short of thermal equipartition so it cannot easily affect the dynamical evolution of the star. This is demonstrated in Figure 6 which shows the mass density weighted average of the inverse plasma beta ( $1/\beta_B$ ) inside the star. In all cases the increase of magnetic pressure saturates at a level that is significantly less than 10% of the thermal pressure averaged across the star (with maximum peak values of about 4% for the  $64^3$  runs, and 6% for the high resolution  $96^3$  case). It appears that field saturation is determined by universal behavior in the partitioning of thermal and magnetic energy, independent of initial amplitude. This is true also for the  $\Gamma = 2$  and 3 cases, both of which result in mean  $1/\beta_B$  profiles similar to the  $\Gamma = 5/3$  results shown in Figure 6.

Consequently, we do not expect gravitational waveforms to be affected appreciably by toroidal magnetic fields, as we demonstrate in Figure 7 for the  $\Gamma = 5/3$  cases, Figure 8 for  $\Gamma = 2$ , and Figure 9 for  $\Gamma = 3$ . Figures 7 through 9 plot the quantity  $rh+$  normalized by the scale factor  $(GM/\varpi_E c^2)^2$ . Figure 9 also includes results from a poloidal initial field configuration (run PG30B100) for comparison. Figure 7 (corresponding to the  $\Gamma = 5/3$  cases) closely resembles Figure 9 of New et al. (2000): we match the amplitude and frequency of oscillations and find that our results are intermediate between the “D1” and “L1” displays in duration and pattern of the wave signal. It is not until the field strength is increased to  $1/\beta_{B,\min} \sim 1$  with locally comparable thermal and magnetic pressures that we observe amplitude deviations of order 30% in Figure 7.

The first evidence of oscillations in Figure 7 occurs at time  $t \sim 6$  which corresponds to the instant when the  $m = 2$  mode first begins to dominate the spectral signal in Figure 2. The global envelope shape (essentially the overall amplitude) of the gravitational wave emission tracks nicely the growth and eventual decay of the  $m = 2$  mode curve in Figure 2. Maximum peaks in both wave signals and spectral mode profiles correlate precisely at time  $t \sim 16$ , and both exhibit comparable rise and decay times. Another point of interest in comparing Figures 7 – 9 is the apparent trend for the start of the wave signals to be delayed with increasing adiabatic index  $\Gamma$  (evident also in the spectral mode plots). However, we have found that the onset of the instability is sensitive to a number of numerical factors (e.g., grid resolution, Courant factor), and it is difficult to make quantitative conclusions regarding this effect. For example, the magnetized and unmagnetized  $\Gamma = 5/3$  high-resolution cases resemble Figure 7 but for a slight delay of about 1.5 dynamical times, effectively a 10% temporal shift in the waveform. However, other aspects of the waveforms are similar between the higher and lower resolution cases: the magnetized results are essentially identical to the unmagnetized waveforms, and the wave amplitudes agree nicely.

Even though the gravitational wave amplitudes are fairly consistent with no obvious correlation with  $\Gamma$  (approximately 0.45, 0.35, and 0.44 for  $\Gamma = 5/3$ , 2 and 3, respectively), the wavelength of perturbations between the two biggest wave crests and the burst duration (between leading and trailing wave crests with amplitude larger than 0.1) do appear to increase monotonically with  $\Gamma$ . In particular, we find wavelengths of approximately  $3.1\hat{t}$ ,  $4.0\hat{t}$ , and  $4.8\hat{t}$  for  $\Gamma = 5/3$ , 2, and 3, a fractional increase (in wavelength) of about 20% between  $\Gamma = 2$  and  $\Gamma = 5/3$ , and about 55% between  $\Gamma = 3$  and  $\Gamma = 5/3$ . Trends in both amplitudes and wavelengths are consistent with those of Houser & Centrella (1996), who find the amplitude is independent of the polytropic index, but  $\Gamma = 2$  ( $\Gamma = 3$ ) fluids generate gravitational waves with 20% (58%) longer wavelengths than  $\Gamma = 5/3$ .

We cannot quantify the burst duration as easily since the late time solutions can be inaccurate due to buildup of numerical errors, and sensitivity to computational parameters (e.g., Courant factor, artificial viscosity constants). However, a comparison of Figures 7 – 9 clearly shows a lengthening of the pulse duration by more than 50% as the models grow stiffer. Such behavior was observed also by Houser & Centrella (1996) and Williams



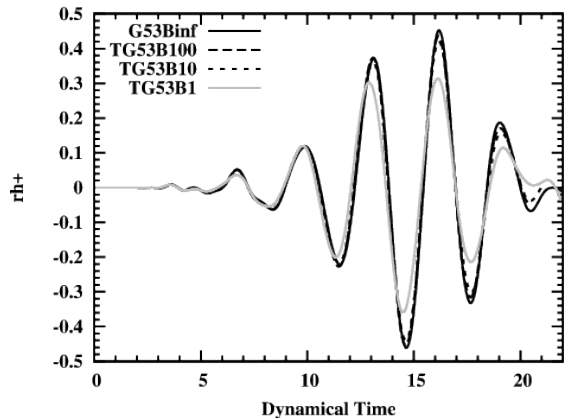


FIG. 7.— Gravitational waveforms ( $rh+$ ) extracted from several magnetized and unmagnetized  $\Gamma = 5/3$  cases. The horizontal time axis is displayed in dynamical code units  $\sqrt{\varpi_E^3/GM}$ , and the wave amplitude is normalized by  $(GM/\varpi_E c^2)^2$ .

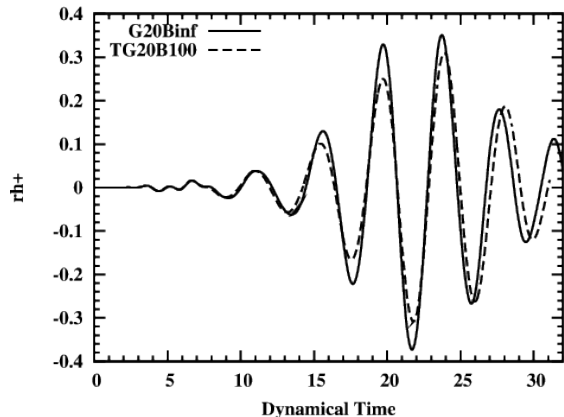


FIG. 8.— Gravitational waveforms with magnetic fields (dashed line) and without (solid line) for  $\Gamma = 2$ .

& Tohline (1988) in their unmagnetized studies: stiffer polytropes produce more elongated bars, rotate more slowly, and undergo more periods of spiral arm ejection and core recontraction, resulting in longer bursts of gravitational wave signals. The addition of toroidal magnetic fields to the stellar profile does not appear to affect these behaviors appreciably as the burst duration is generally shorter than the timescale  $t_B$  for magnetic braking to take effect:  $t_B \sim \varpi_E/v_A \gtrsim 25$ -50 dynamical (code) units at the field saturation time for all of the cases we have considered.

### 3.2. Poloidal Magnetic Field Configurations

Unlike the cases which start from initially toroidal magnetic field configurations, simulations performed of models which begin with poloidal fields evolve differently than unmagnetized cases if the initial field amplitude is large. In particular, we found little qualitative difference between all the toroidal calculations at both low ( $64^3$ ) and high ( $96^3$ ) grid resolutions, regardless of initial field amplitude. For this reason, all of the results presented in Section 3.1 corresponded to low-resolution cases, with the added advantage of allowing for many different parameter combinations to be investigated. However, for the poloidal cases, we observed an increased sensitivity to spatial resolution as well as a growing impact on bar for-

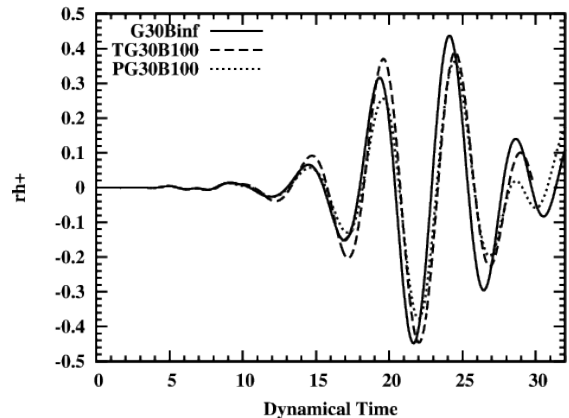


FIG. 9.— Gravitational waveforms with magnetic fields (dashed lines) and without (solid line) for  $\Gamma = 3$ .

mation with increasing field strength, especially for the two largest amplitude cases (PG53B100 and PG53B10). All poloidal results presented in this section are therefore shown at high ( $96^3$ ) grid resolution.

To illustrate the effect of the magnetic field on bar formation, Figure 10 shows images of the mass density (for the G53BInfHR case) and magnetic pressure (for the cases PG53B100HR with  $\beta_{B,\min} = 100$ , and PG53B10HR with  $\beta_{B,\min} = 10$ ), all in the equatorial plane. All three sets of images display the same contour levels of the mass density (0.5, 0.05, 0.005, and 0.0009), normalized to the initial maximum mass density  $\rho_{\max,0}$ . Images making up the left column for the case without a magnetic field are shown at times  $t=15$ , 17, and 21; images in the center column are shown for case PG53B100HR at times  $t=17$ , 19, and 23; and images in the right column are shown for case PG53B10HR at times  $t=15$ , 17, and 19, all in dynamical (code) units. The PG53B100HR images are shown at later times than those for the unmagnetized case to illustrate that a bar forms with a shape similar to the no-field case, but delayed approximately two dynamical times. For the higher magnetic field strength run, PG53B10HR, there is no indication that a structure resembling a bar is going to form at this resolution, a point we return to below.

The effect of an initially poloidal magnetic field on the growth of the bar mode is quantified in the nonaxisymmetric amplitudes  $|A_m|$ , computed as described above in Section 3.1. In Figures 11 and 12, we plot the evolution of the amplitudes  $|A_m|$  of the  $m = 2$  and  $m = 4$  modes, respectively, for runs G53BInfHR, PG53B500HR, PG53B100HR, and PG53B10HR. It is apparent that for the lowest field case (PG53B500HR), the magnetic field has little effect on the growth of either mode, but increasing the field amplitude systematically suppresses the different modes. For example, the intermediate field case (PG53B100HR) exhibits growth similar to the no-field case but with a temporal delay and slightly smaller mode amplitudes, while modes in the highest field amplitude case (PG53B10HR) are suppressed by approximately two orders of magnitude relative to the no-field case. Although not shown, we note that the  $m = 1$  and  $m = 3$  modes are similar to those observed in the toroidal cases, in that they saturate at levels which are well below the characteristic  $m = 2$  and 4 profiles of the bar mode.

We expect the gravitational waveforms produced in

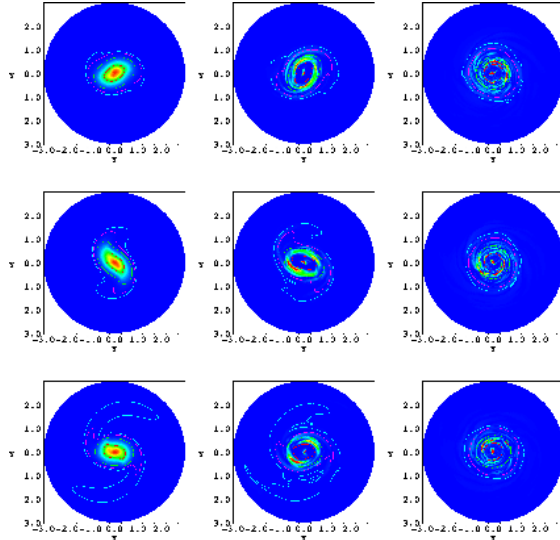


FIG. 10.— Development of the bar-mode in  $\Gamma = 5/3$  simulations with initially poloidal magnetic fields (PG53B100HR, center column, and PG53B10HR, right column) and without (G53BInfHR, left column). Rows represent snapshot solutions at different times:  $t = 15, 17,$  and  $21$  for the case without magnetic fields,  $t = 17, 19,$  and  $23$  for the PG53B100HR case, and  $t = 15, 17,$  and  $19$  for the PG53B10HR case, all in dynamical (code) units ( $\tilde{t} = \sqrt{\varpi_E^3/GM}$ ). Contour levels represent mass density in the equatorial plane at four values normalized to the initial maximum density  $\rho_{\max,0}$ : (0.5, 0.05, 0.005, and 0.0009). Linear color maps represent mass density in the case without magnetic fields (left column), and magnetic pressure in the cases with fields (center and right columns). The magnetic pressure color scale is fixed for all the images to cover the range  $0 \rightarrow 10^{-3}$ .

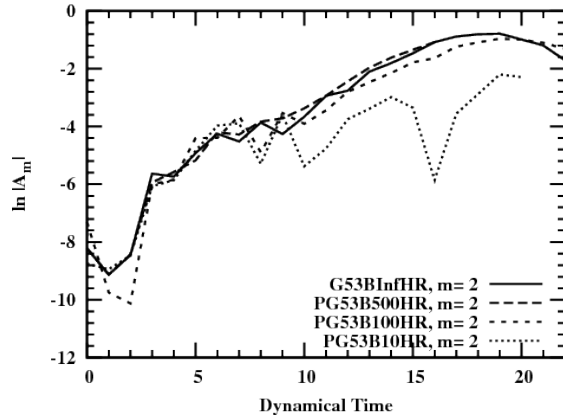


FIG. 11.— Growth of the  $m = 2$  azimuthal Fourier mode amplitudes  $|A_m|$  in the mass density, comparing four  $\Gamma = 5/3$  cases: unmagnetized (G53BInfHR, dark line) and magnetized, with initially poloidal magnetic fields (PG53B500HR, long dashed line; PG53B100HR, short dashed line; and PG53B10HR, dotted line). Results are derived by averaging the density inside a ring centered at  $\varpi = 0.45\varpi_E$  in the equatorial plane and extending one zone deep in both radial and polar directions.

each of these runs to reflect what is seen in the density profiles and the mode amplitude plots. In Figure 13, we show the quantity  $rh_+$  normalized by the scale factor  $(GM/\varpi_E c^2)^2$ , for runs G53BInfHR, PG53B500HR, PG53B100HR, and PG53B10HR. For the plot shown, the low-amplitude field case PG53B500HR has been shifted back 0.2 dynamical times, and the moderate-amplitude field case PG53B100HR has been shifted 1.4 dynamical times so that the maximum of the first large peaks

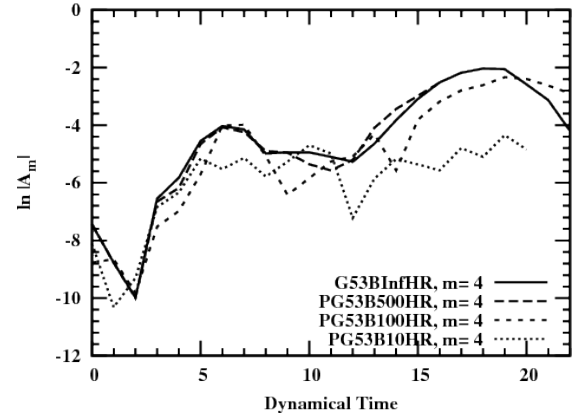


FIG. 12.— Growth of the  $m = 4$  azimuthal Fourier mode amplitudes  $|A_m|$  in the mass density, comparing four  $\Gamma = 5/3$  cases: unmagnetized (G53BInfHR, dark line) and magnetized, with initially poloidal magnetic fields (PG53B500HR, long dashed line; PG53B100HR, short dashed line; and PG53B10HR, dotted line). Results are derived by averaging the density inside a ring centered at  $\varpi = 0.45\varpi_E$  in the equatorial plane and extending one zone deep in both radial and polar directions.

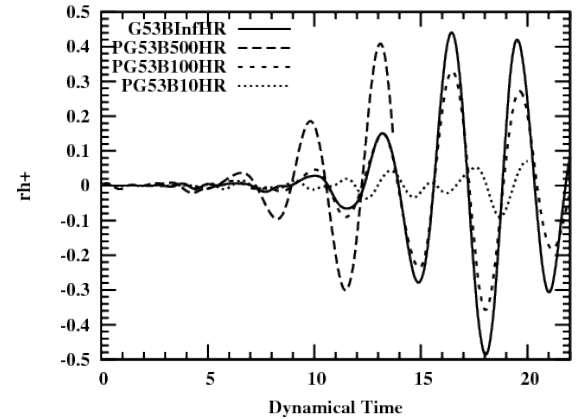


FIG. 13.— Gravitational waveforms ( $rh_+$ ) extracted from four  $\Gamma = 5/3$  cases: unmagnetized (G53BInfHR, dark line) and magnetized, with initially poloidal magnetic fields (PG53B500HR, long dashed line; PG53B100HR, short dashed line; and PG53B10HR, dotted line). In this plot, the waveforms produced in the PG53B500HR and PG53B100HR simulations have been shifted in time so that the peaks in the waveforms line up with those of the unmagnetized case.

line up. As expected, waveforms exhibit systematically smaller amplitudes and greater temporal delays with increasing initial field amplitude.

In Figure 14, we plot the inverse plasma beta ( $1/\beta_B$ ), azimuthally averaged over the ring at  $\varpi = 0.65\varpi_E$  in the equatorial plane, for runs PG53B500HR, PG53B100HR, and PG53B10HR. For the lowest field case (PG53B500HR), in which the dynamics are affected only slightly, the magnetic pressure is never more than about 4% of the fluid pressure in this ring. However, for the highest field case (PG53B10HR), in which the bar mode is completely suppressed, the magnetic pressure is already just below 4% of the fluid pressure in the initial configuration, and peaks at around 80% of the fluid pressure within five dynamical times before leveling off again at  $\sim 4\%$ . Under these conditions, we would expect the magnetic field to have a significant effect on the overall evolution of the star.

We can understand the immediate onset of the field

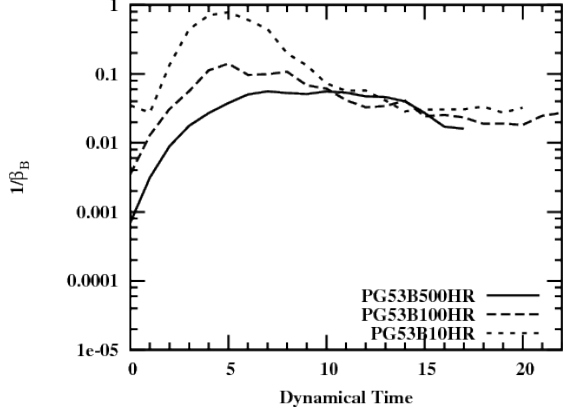


FIG. 14.— Inverse of the magnetic plasma beta ( $1/\beta_B$ ) azimuthally averaged over a ring in the equatorial plane at the radius  $0.65\varpi_E$ .

amplification observed in Figure 14 by considering the evolution of individual components of the magnetic field. In Figure 15, we plot  $8\pi$  times the magnetic pressure, as well as the contributions to this quantity from each of the three cylindrical components of the magnetic field, all azimuthally averaged over the ring at  $\varpi = 0.65\varpi_E$  in the equatorial plane, for runs PG53B500HR, PG53B100HR, and PG53B10HR. For all three cases, we see that the increase in the overall magnetic pressure tracks the increase in the azimuthal contribution to that pressure. This behavior, in addition to the immediate field amplification, is characteristic of the  $\Omega$ -dynamo, which one would expect to be active with a poloidal magnetic field present. This effect can be seen qualitatively in Figure 16, in which we show magnetic field lines at early times for the PG53B100HR case. The magnetic field lines, as well as mass density contours, are shown at times  $t = 0, 1, 2,$  and  $3t$ . The field lines show immediate and dramatic stretching in the azimuthal direction, contributing to the field amplification observed in Figures 14 and 15.

Another important point from Figure 14 is that the late time saturation level of  $1/\beta_B$  is approximately the same in all three simulations. A similar behavior and level of saturation are evident in Figure 6 for the toroidal cases. This remarkable independence from the initial field strength and orientation is important, as it indicates that a common and robust physical mechanism is at play setting the final saturation level. Also, we see from Figure 15 that the final magnitude of the azimuthal component ( $g_{\phi\phi}B^\phi B^\phi$ ) is approximately the same in all three simulations, and the second most significant component, the radial one ( $g_{\eta\eta}B^\eta B^\eta$ ), always finishes within an order of magnitude of the azimuthal component. This suggests that these two components have either achieved a static final configuration common to all the simulations, or they are feeding off of one another and exchanging energy with the gas through some equilibrium process. The latter is consistent with expectations of the MRI, which gradually takes over as the  $\Omega$ -dynamo saturates, and which is expected to be active in all of our stellar models according to criterion (Equation (18)).

We end this section with a few words of caution regarding the convergence of results for those cases run with poloidal initial fields. The smallest B500 case is reasonably converged between low ( $64^3$ ) and high ( $96^3$ ) grid resolutions, resulting in nearly identical gravitational wave

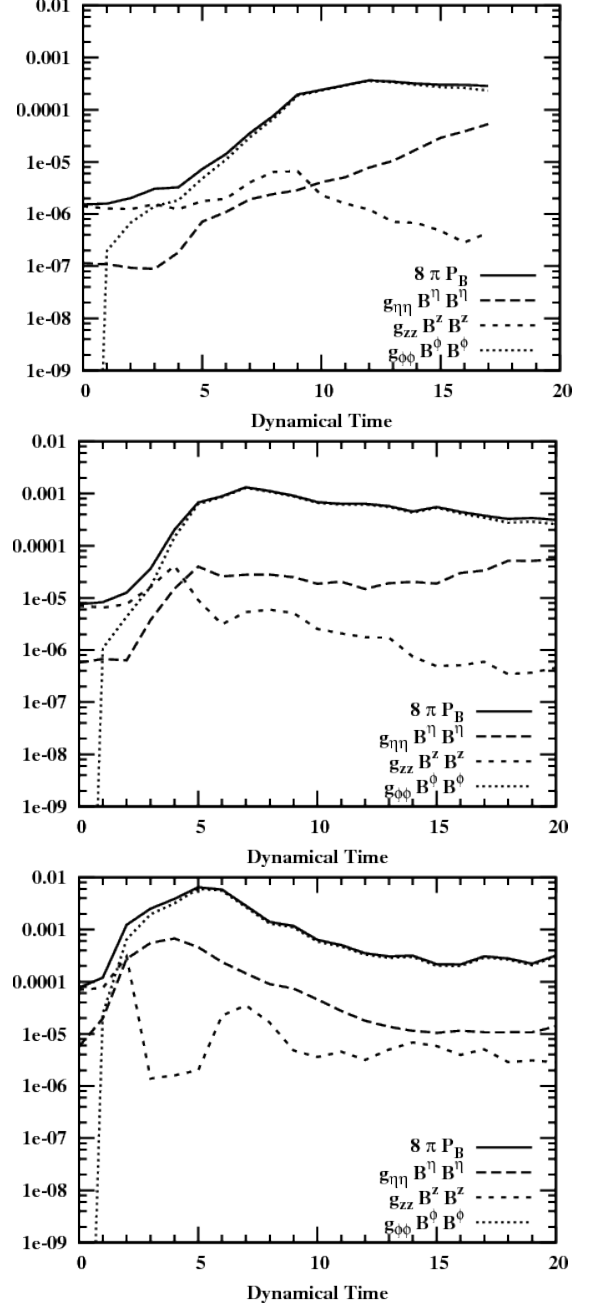


FIG. 15.— We show  $8\pi$  times the magnetic pressure, as well as the contributions to this quantity from each of the three cylindrical components of the magnetic field, all azimuthally averaged over the ring at  $\varpi = 0.65\varpi_E$  in the equatorial plane, for runs PG53B500HR (top), PG53B100HR (center), and PG53B10HR (bottom).

frequencies and maximum peak differences of about 25% in amplitude. However, the intermediate B100 case exhibited vastly different solutions at low and high resolutions. The bar mode was essentially suppressed completely at low resolution, but managed to form nicely at  $96^3$  zones, demonstrating the sensitive and demanding nature of these calculations. We cannot therefore be certain that the largest amplitude (B10) case is fully converged and does not form a bar. It would require even larger computational grids to confirm this result, something that is beyond our current allocation resources. At issue is the resolution of the winding of the field lines

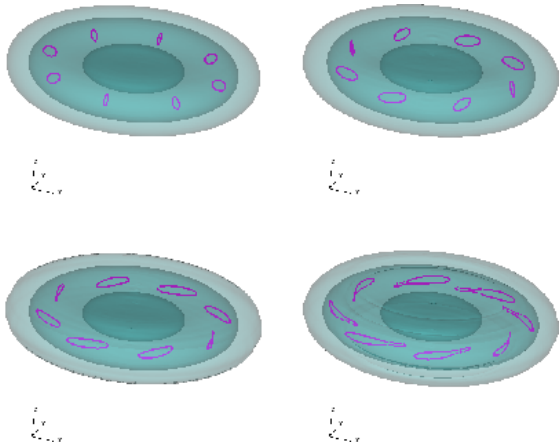


FIG. 16.— Magnetic field lines for the PG53B100HR simulation, at times 0 and  $1 \tilde{t}$  (top row), and 2 and  $3 \tilde{t}$  (bottom row). Also shown are mass density contours at three values, normalized to the initial maximum density  $\rho_{\max,0}$ : (0.5, 0.05, 0.005).

as the star rotates, the accurate capturing of reconnection events, and mostly the severe restrictions placed on the stability time step from magnetically dominated MHD and fast Alfvén velocities as the field works its way through the stellar atmosphere.

#### 4. CONCLUSIONS

We have studied the growth of the dynamical bar-mode instability in differentially rotating magnetized neutron stars through a set of numerical Newtonian MHD calculations. The calculations explored both toroidal and poloidal initial field distributions of differing strengths, as well as the role of the equation of state.

For our initially toroidal field configurations, field amplification always saturated at a level insufficient to strongly affect the dynamics of the bar mode. Even the most extreme case (TG53B1,  $\beta_{B,\min} = 1$ ), with equal initial magnetic and hydrodynamic pressures within the toroidal loop, gave only a  $\sim 30\%$  change in gravitational wave properties. Otherwise evolution proceeded quite similarly to our unmagnetized reference cases.

The effects were larger for the poloidal configurations. In the most extreme case considered (model PG53B10HR with  $\beta_{B,\min} = 10$ ), the magnetic field was sufficient to completely suppress the formation of a bar. However, in that case, we started with the magnetic field already within a factor of  $\sim 30$  of being dynamically more important than thermal pressure in some portions of the

star. It then only took a few dynamical times of field growth for  $\beta_B$  to approach unity, a timescale that is much shorter than the bar deformation time for azimuthal Fourier modes to reach appreciable amplitudes. Also, due to the computationally demanding nature of evolving strong poloidal fields, we cannot verify that this result will not change with increased grid resolution. For less extreme initial conditions, the effects of including poloidal field components were consistently more modest with decreasing initial field amplitude. These lower amplitude calculations are also less demanding computationally and can, like the toroidal cases, be more easily checked for convergence. The principle effects of introducing poloidal fields are in systematically delaying the onset of the bar mode and in suppressing both Fourier mode and gravitational wave amplitudes, all of which become negligible with initial field amplitudes below the threshold of  $1/\beta_{B,\min} \lesssim 10^{-2}$ .

Overall, our results suggest that the effect of magnetic fields on the emergence of the bar-mode instability in neutron stars is not likely to be very significant. Particularly considering that collapse progenitor models predict realistic field configurations that are dominantly toroidal in nature with toroidal and poloidal components of order  $10^{10}\text{G}$  and  $10^6\text{G}$ , respectively (Heger et al. 2005), substantially below most of the field configurations we have considered. Thus, except in special cases where neutron stars are born very highly magnetized, we might still expect them to be good gravitational wave sources if their rotational kinetic energies exceed the critical bar-mode instability parameter.

Computations were performed at the Barcelona Supercomputing Center (BSC) under activity AECT-2007-3-0002, the Lawrence Livermore National Laboratory (LLNL), the College of Charleston (CoC), and at the High Performance Academic Computing Environment at Washburn University (HiPACE). This work was performed in part under the auspices of the U.S. Department of Energy by Lawrence Livermore National Laboratory under contract no. DE-AC52-07NA27344. P.C.F. gratefully acknowledges the support of the College of Charleston 4th Century Initiative and the South Carolina Space Grant Consortium. J.A.F. acknowledges financial support from the Spanish Ministry of Education and Science (AYA 2007-67626-C03-01).

#### REFERENCES

- Anninos, P., & Fragile, P. C. 2003, *ApJS*, 144, 243  
 Anninos, P., Fragile, P. C., & Murray, S. D. 2003, *ApJS*, 147, 177  
 Anninos, P., Fragile, P. C., & Salmonson, J. D. 2005, *ApJ*, 635, 723  
 Baiotti, L., Giacomazzo, B., & Rezzolla, L. 2008, *Phys. Rev. D*, 78, 084033  
 Baiotti, L., Pietri, R. D., Manca, G. M., & Rezzolla, L. 2007, *Phys. Rev. D*, 75, 044023  
 Balbus, S. A., & Hawley, J. F. 1991, *ApJ*, 376, 214  
 Burrows, A., Dessart, L., Livne, E., Ott, C. D., & Murphy, J. 2007, *ApJ*, 664, 416  
 Cerdá-Durán, P., Font, J. A., Antón, L., & Müller, E. 2008, *A&A*, 492, 937  
 Chandrasekhar, S. 1969, *Ellipsoidal figures of equilibrium* (The Silliman Foundation Lectures; New Haven, CT: Yale Univ. Press)  
 Dedner, A., Kemm, F., Kroner, D., Munz, T., C. D. Schnitzer, & Wengenberg, M. 2002, *J. Comput. Phys.*, 175, 645  
 Dimmelmeier, H., Ott, C. D., Marek, A., & Janka, H.-T. 2008, *Phys. Rev. D*, 78, 064056  
 Finn, L. S., & Evans, C. 1990, *ApJ*, 351, 588  
 Fragile, P. C., Anninos, P., Gustafson, K., & Murray, S. D. 2005, *ApJ*, 619, 327  
 Hachisu, I. 1986, *ApJS*, 61, 479  
 Heger, A., Woosley, S. E., & Spruit, H. C. 2005, *ApJ*, 626, 350  
 Houser, J. L., & Centrella, J. M. 1996, *Phys. Rev. D*, 54, 7278  
 Houser, J. L., Centrella, J. M., & Smith, S. C. 1994, *Phys. Rev. Lett.*, 72, 1314  
 Jackson, J. D. 1975, in *Classical Electrodynamics* (2nd ed.; New York: Wiley)  
 Liu, Y. T. 2002, *Phys. Rev. D*, 65, 124003

- New, K. C. B., Centrella, J. M., & Tohline, J. E. 2000, Phys. Rev. D, 62, 064019
- Ott, C. D., Burrows, A., Thompson, T. A., Livne, E., & Walder, R. 2006, ApJS, 164, 130
- Ott, C. D., Dimmelmeier, H., Marek, A., Janka, H.-T., Hawke, I., Zink, B., & Schnetter, E. 2007, Phys. Rev. Lett., 98, 261101
- Shibata, M., Baumgarte, T. W., & Shapiro, S. L. 2000, ApJ, 542, 453
- Shibata, M., Karino, S., & Eriguchi, Y. 2002, MNRAS, 334, L27
- Shibata, M., Karino, S., & Eriguchi, Y. 2003, MNRAS, 343, 619
- Spruit, H. C., & Phinney, E. S. 1998, Nature, 393, 139
- Williams, H., & Tohline, J. 1988, ApJ, 334, 449
- Woosley, S. E., & Heger, A. 2006, ApJ, 637, 914